Bio-originated mesosilicate SBA-15: synthesis, characterization, and application for heavy metal removal

Check for updates

Wensheng Yang[1], Saeed Shirazian [2,3] ✉, Roozbeh Soltani [4] & Masoud Habibi Zare[5]

In the path of walking on the road of sustainable and eco-friendly production methods for manufacturing nanomaterials and utilizing them in environmental applications, this article deals with the prosperous synthesis of a biogenic cyclam-functionalized homologous SBA-15 (BCFH-SBA-15). For this purpose, the agricultural waste of the extensively consumed sorghum was used as a rich source of silica in the preparation of BCFH-SBA-15 with a bimodal micro-mesoporous architecture and a substantial surface area of 325 $m^2 g^{-1}$ through a simple one-pot environmentally friendly approach. The material was structurally characterized through the use of different instrumental analyses such as XRD, FTIR, FESEM, TEM, and nitrogen adsorption/desorption isotherms. BCFH-SBA-15 proved to be highly efficient in adsorbing Ni(II) in aqueous solutions, as confirmed by the most reliable classical models utilized for determining isotherm, thermodynamic, and kinetic adsorption parameters. The Langmuir isotherm model provided the most accurate representation of the experimental results, and it was used to calculate the maximum adsorption capacity of BCFH-SBA-15 under optimal conditions (pH = 6.0, adsorbent dose = 3.00 mg, contact time = 20 min). The maximum adsorption capacity at four temperatures of 298, 303, 308, and 313 K was estimated to be 243.36, 253.87, 260.95, and 266.28 $mg\ g^{-1}$, respectively; surpassing most previously reported adsorbents for Ni(II) adsorption. The thermodynamic data of Ni(II) adsorption on the BCFH-SBA-15 indicated a strong chemisorption ($\triangle H^{o}_{ads.} = +122.61\ kJ\ mol^{-1}$) and spontaneous process ($\triangle G^{o}_{ads.} = -29.161$ to $-36.801\ kJ\ mol^{-1}$) with a low degree of randomness ($\triangle S^{o}_{ads.} = 0.5093\ kJ\ mol^{-1}\ K^{-1}$).

Nanomaterials encompass a diverse range of structures, including nano-porous silicates and carbon materials[1], carbonaceous and non-carbonaceous nanotubes[2,3], metal oxides and metal hydroxides[4], metal-organic frameworks[5], porous organic polymers[6], as well as nanoparticle reinforced polymer composites[7]. These materials have demonstrated remarkable potential in a multitude of applications such as water remediations[8], extraction[9], catalysis[10], drug delivery[11], tissue engineering[12], wound healing and self-healing intelligent composites[13,14], electronic devices[15], etc. Both experimental and theoretical studies have contributed to our understanding of thsee materials, driving advancement and innovations. It is important to acknowledge that in the past years, special attention has been paid to the further development of nanomaterials from the perspective of environmentally friendly synthesis and green chemistry, using strategies in line with the concept of sustainable development[16–18].

Silica is a very important and vital compound on our planet, traces of which can be found in the mechanisms of life and living organisms, right down to a wide variety of mineral structures and its wide application in the modern world. It is worth mentioning that due to the abundance of silica in the earth's crust, its processability, and its non-toxicity for living organisms and human beings, the use of silica compounds for the preparation of practical materials, especially in the form of nanomaterials, will attract more and more attention from research and industrial centers. NSPs are among the most famous and applicable nanoporous materials and have attracted a great deal of interest due to their excellent physico-chemical properties such as high surface, large pore volume, tailorable pore size, good hydrothermal-mechanical stability, and functionaliz-ability. It is not surprising that these materials have found their applications in the fields of drug delivery, catalysis, adsorption/extraction,

[1]College of Chemistry and Chemical Engineering, Yulin University, Yulin, Shaanxi, China. [2]Institute of Research and Development, Duy Tan University, Da Nang, Vietnam. [3]School of Engineering and Technology, Duy Tan University, Da Nang, Vietnam. [4]Independent Researcher, Halifax, Nova Scotia, Canada. [5]Isfahan University of Technology, Department of Chemical Engineering, 84156-83111 Isfahan, Iran. ✉e-mail: saeedshirazian@duytan.edu.vn

anti-corrosion materials, electronic devices, imaging agents, etc. during the last four decades[19–22].

However, providing the source of silica for the synthesis of the NSPs family has remained a challenge from both environmental and economic points of view. Alkyl orthosilicates, viz. tetraethyl orthosilicate, tetramethyl orthosilicate, and polyethlydiorthosilicate, have been used as commercial silica sources for the preparation of NSPs during the past few decades. Nevertheless, researchers are looking to replace these synthetic silica sources with greener and more environmentally friendly silica sources, or in other words an eco-design for the sustainable production of silica[23]. The most important and up-to-date alternative source is to use of agricultural residues that contain silica in their herbal structure, and we call them sustainable biobased (biogenic) silica gel (SBSG). However, there are still challenges in the way of using SBSG as a green and environmentally friendly source for the synthesis of NSPs, including the need for a pure silica source formulation and homogeneous composition for the synthesis of NSPs (because the synthesis of NSPs strongly depends on the purity of the starting materials such as silica source). Therefore, looking at a synthetic strategies based on sustainable development and trying to reduce prices and increase production both qualitatively and quantitatively in line with the use of SBSG as a silica source, as well as increasing knowledge and skills to use renewable herbal resources such as agricultural waste for the preparation of SBSG should be prioritized.

Sorghum (Guinea corn) is the fifth most important cereal crop (wheat, rice, maize, pearl millet, and sorghum) with regard to both harvested area and worldwide production, providing over half of the world's food calories (about 44%) consumed per capita globally[24]. Sorghum is more resistant to high temperatures and drought conditions, two environmental factors in the future that are expected to intensify gradually, in comparison to the other four cereal crops[25]. Accordingly, the agricultural waste resulting from the harvest of sorghum annually accounts for a significant amount, which can be considered as a potential SBSG source for the preparation of NSPs, which is not only more affordable in terms of economy and production costs but also in line with environmental policies and green chemistry perspective. The sorghum grasses have the capability to accumulate silica in the form of silicic acid, which can be transformed into amorphous rigid silica with an impressive purity of 95-96%, commonly known as micro-silica phytoliths, through a chemical extraction process by using acid or base hydrolysis under high-temperature pressurized condition followed by calcination[26,27].

The utilization and valorization of sorghum agricultural residues have attracted increasing interest in recent years owing to their potential as a sustainable and renewable resource. These residues offer significant opportunities for waste valorization and resource recovery, contributing to the development of a circular economy[16]. However, the emphasis on the utilization and valorization of sorghum agricultural residues for the preparation of functionalized silica-based adsorbents has been lacking in previous studies. In this study, we aim to address this gap by investigating the potential of sorghum agricultural residues as an adsorbent for the removal of Ni(II) from contaminated water sources.

Ni(II) has emerged as a pervasive water pollutant in our locality, primarily originating from industrial activities and anthropogenic sources. Furthermore, Ni(II) exhibits unique characteristics that differentiate it from other HMs, including its ability to form stable complexes and its moderate to high toxicity towards aquatic organisms. The choice of Ni(II) as the pollutant of interest in our study is motivated by its significance as a water pollutant in our region (Iran, Esfahan, Zayandeh Rood), its distinct recalcitrance in water compared to other HMs (when compared to other HMs, the concentration of Ni(II) and Cd(II) exceeds the EC standard)[28], and the presence of components within our adsorbent that have demonstrated a high affinity and selectivity for Ni(II). By investigating the adsorption behavior of sorghum agricultural residues towards Ni(II), we aim to contribute to the development of efficient and selective adsorbents for the removal of this pollutant, thereby addressing the challenges associated with Ni(II) contamination in water sources.

Generally, to increase the efficiency of NSPs and improve their surface properties, their surface structure is treated with chemical agents called SCAs before use[29]. For surface modification, there are two general methods called post-grafting and one-pot co-condensation (direct synthesis), in the first one, the SCA is attached to the silica surface after the SNPs preparation and in a separate step, and in the second method, SCA is added during the SNPs preparation process. It is worth emphasizing that, to the best of our knowledge, most of the reports related to the functionalization of NSPs and SBSG-based NSPs have used the post-grafting method[30]. In other words, most researchers have focused more on the use of different SBSG and less attention has been paid to the type of functionalization method. Interestingly, there are many reports regarding the importance of the modification methods in preparation of various kinds of nanomaterials such as NSPs, and their significant impact on the performance of the synthetic material because of the influences that each method has on the physicochemical features including surface area, pore accessibility, hydrothermal and mechanical resistances as well as synthesis time (which in turn has a direct impact on production costs)[31,32]. The utilization of NSPs as absorbents, catalysts, or drug carriers poses a significant challenge, particularly when striving to achieve a uniform surface functional group distribution, and it is highly recommended to utilize NSPs possessing a surface featuring more homogeneous functional groups. One of the main disadvantages of the post-grafting method is the uncontrollable distribution of the SCAs on the surface of the NSPs, which causes non-uniformity of the adsorption/active sites on the surface[33].

To address all the above propositions and consider an environmentally friendly synthetic strategy, a green synthesis protocol for the preparation of biogenic ordered NSPs with bimodal micro-mesoporosity and organo-functionalized surface has been reported in which the source of silica is provided by a simple green protocol from the sorghum husk ash (SHA) within the context of sustainable chemistry. The synthesized biogenic cyclam-functionalized homologous-SBA-15 (abbreviated as BCFH-SBA-15) was fully characterized by different methods such as powder low-angle XRD, FTIR, FESEM, TEM, and nitrogen adsorption-desorption and used as a superior green adsorbent for the removal of Ni(II) as an example of toxic heavy metals from aqueous solution. Cyclam is classified as an aza-crown ether and was selected as a potential adsorptive functional group on the surface of BCFH-SBA-15.

Results and discussion
Synthesis procedure

A schematic representation of the process for preparing the BCFH-SBA-15 adsorbent with Na_2SO_3 solution derived from SHA is given in Fig. 1. Sorghum, being a highly cultivated agricultural product, generates a considerable amount of agricultural waste, while simultaneously providing a renewable source for silica preparation due to its rich silica content in its plant structure. As depicted in Fig. 1, Na_2SO_3 solution was first prepared through acid digestion of sorghum in a stainless steel autoclave under relatively high pressure-temperature conditions followed by calcination of SHA in an air atmosphere and, subsequently, the reaction of resulting amorphous silica and NaOH. BCFH-SBA-15 was synthesized through a facile one-pot synthesis method in which P123, Na_2SiO_3, and HCl were used as a soft templating agent, a sustainable silica source, and a hydrolyzing agent, respectively. In this method, SCA-bearing cyclam, 1-(3-(trimethoxysilyl)propyl)-1,4,8,11-tetraazacyclotetradecane, is added to the reaction mixture during the formation of the organic template. Upon the introduction of acid to the aqueous solution containing the surfactant (P123, templating agent) and the subsequent complete dissolution of the P123 molecules, the formation of cylindrical micelles of the template is initiated. The positioning of the hydrophilic head group and hydrophobic tail of P123 molecules in a micelle is such that they are regularly aligned cylindrically with the head group facing outward and the tail facing inward. Through the addition of Na_2SO_3 and SCA-bearing cyclam, the density of the silica network surrounding the organic template increases as a result of the hydrolysis
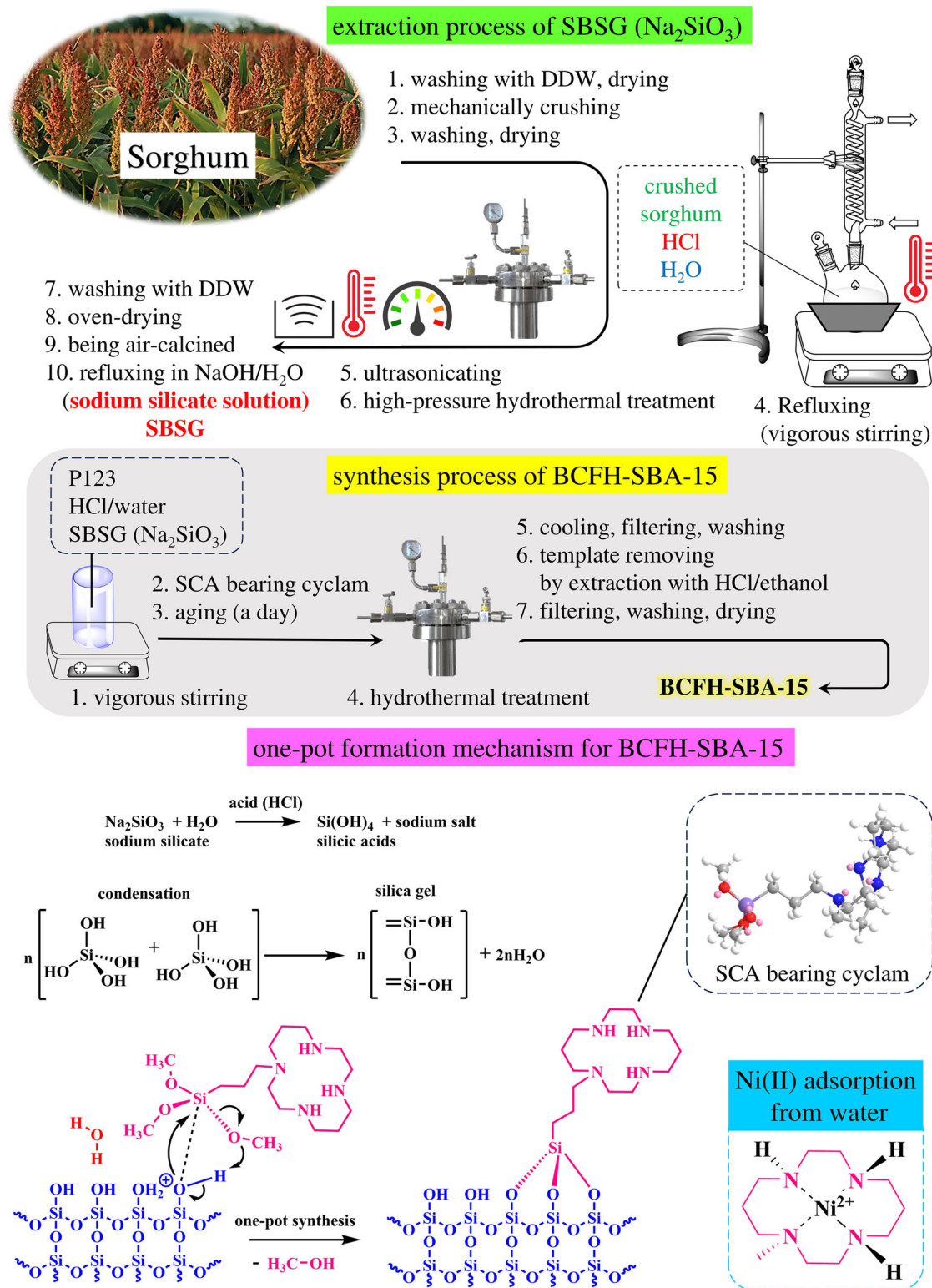
Fig. 1 | Preparation and application of BCFH-SBA-15 for Ni(II) removal. Schematic figure of the preparation route of BCFH-SBA-15 from the one-pot synthesis method using silica extraction from SHA and its application as an adsorbent for Ni(II) removal from the aqueous solution.

and condensation of these molecules during the hydrothermal treatment at higher temperatures and pressures.

The one-pot surface modification technique presents a noteworthy advantage over the post-grafting method, in that the SCA molecules are allowed sufficient time to arrange themselves more uniformly within the porous structure of NSPs. As a result, a uniform functionalized surface is obtained throughout the pore structure[34].

Furthermore, this method does not suffer from the pore-blocking phenomenon that is typically observed during surface modification using the first method[35]. This phenomenon is caused by the condensation and attachment of SCAs in the entrance of the channels and pores during hydrolyzing and condensation process, leading to a reduction in active surface area and decreased efficiency of SNPs as adsorbents, catalysts, or carriers[36].
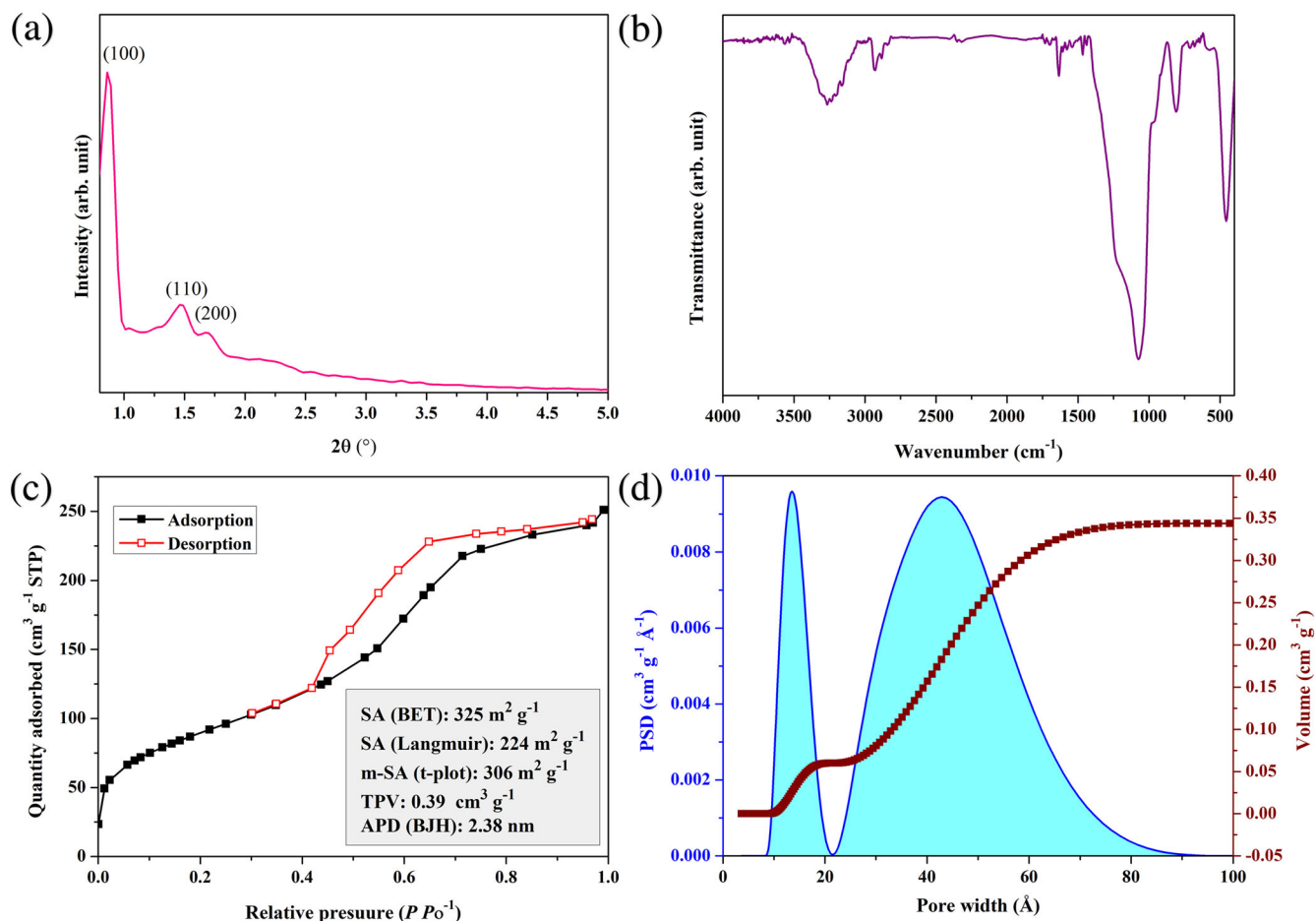
Fig. 2 | Textural analyses of BCFH-SBA-15. XRD pattern (**a**), FTIR spectrum (**b**), nitrogen adsorption-desorption isotherms (**c**), and PSD diagram calculated from the 2D-NLDFT model (**d**) of the BCFH-SBA-15 sample.

Cyclam is a cyclic molecule that is composed of four secondary amines acting as donor centers with sp^3 hybridization with a strong binding affinity toward many transition metal cations such as Ni. The transition metal cation that is chelated by cyclam is situated in the center of the cycle cavity and is coordinated with the nitrogen atoms.

Structure characterization of BCFH-SBA-15

Figure 2a illustrates the XRD pattern of BCFH-SBA-15, which is characterized by a distinct diffraction peak at $2\theta = 0.9°$ and two less prominent peaks at 1.5° and 1.7°, attributed to (1 0 0), (1 1 0) and (2 0 0) reflections, respectively. These observations are indicative of a highly organized p6mm 2D hexagonal mesophase[37]. The XRD diagram obtained at higher 2θ values did not display any reflections, implying that the BCFH-SBA-15 material has an amorphous structure[38].

The FTIR of the sample is depicted in Fig. 2b. All characteristic absorption bands related to the inorganic moiety of BCFH-SBA-15 structure appeared at $804 \, cm^{-1}$ (symmetric stretching vibration of Si-O-Si, medium intensity), $1068 \, cm^{-1}$ and $1220 \, cm^{-1}$ (asymmetric stretching vibration of Si-O-Si, strong intensity), $965 \, cm^{-1}$ (symmetrical silanol, Si-OH, medium intensity), $460 \, cm^{-1}$ (asymmetric bending mode of Si-O-Si), and $1632 \, cm^{-1}$ (H-bonded silanol and adsorbed water O–H bending, weak intensity). Furthermore, a broad absorption band between 3000 to $3500 \, cm^{-1}$ with a medium intensity is attributed to stretching vibrations of –OH (from free silanols and surface adsorbed water) and –NH (from cyclam) functional groups. The stretching mode of C-H bonds of CH_2 and CH_3 groups of SCA-bearing cyclam and the remaining P123 organic chain in the BCFH-SBA-15 structure is characterized by FTIR bands situated at approximately $2880 \, cm^{-1}$ and $2975 \, cm^{-1}$ with weak intensity. The C–N

vibration with weak intensity at about $1605 \, cm^{-1}$ corresponds to the cyclam ring containing C and N atoms indicating the successful grafting of SCA-bearing cyclam to the surface of the silica network. These observations are in complete accordance with the previous reports[36,38–40].

Nitrogen adsorption-desorption of BCFH-SBA-15 shows type-IV isotherm as given in Fig. 2c which exhibits a well-defined hysteresis loop over the relative pressure range from 0.5 to 0.9, indicating capillary condensation of nitrogen in the mesopores. The TPV of BCFH-SBA-15 was estimated to be $0.39 \, cm^3 \, g^{-1}$ and the value of APD according to the BJH model was calculated to be 2.38 nm. The value of SA ($m^2 \, g^{-1}$) of BCFH-SBA-15 according to the BET, Langmuir, and t-plot models was calculated to be 325, 224, and 306, respectively. Based on the data presented, it can be deduced that the available surface area of BCFH-SBA-15 is due to the presence of two specific types of pores - micropores (pores with a diameter of less than 2 nm) and mesopores (pores with a diameter ranging from 2 nm to 50 nm). The micropores, according to the t-plot model, provide a greater surface area (approximately $306 \, m^2 \, g^{-1}$) compared to the mesopores within the material's structure. Therefore, concerning pore shape and structure, the synthesized material can be identified as a homologous SBA-15, exhibiting a highly ordered p6mm 2D bimodal hexagonal micro-mesophase. This conclusion is further supported by the PSD diagram (Fig. 2d), which is based on the 2D-NLDFT calculations. Although the BJH model was once a popular method for determining pore size in nanomaterials, particularly those of the mesoporous variety, the 2D-NLDFT model now offers more precise data regarding the APD of micro-mesoporous materials[41,42]. In this study, the 2D-NLDFT model was utilized to conduct a more precise calculation of the PSD while the BJH model was presented solely for

Fig. 3 | FESEM micrographs. FESEM images of BCFH-SBA-15 (length of scale bars: first row, left = 10 μm; first row, right = 2 μm ; second row, left = 1 μm; second row, right = 200 nm).
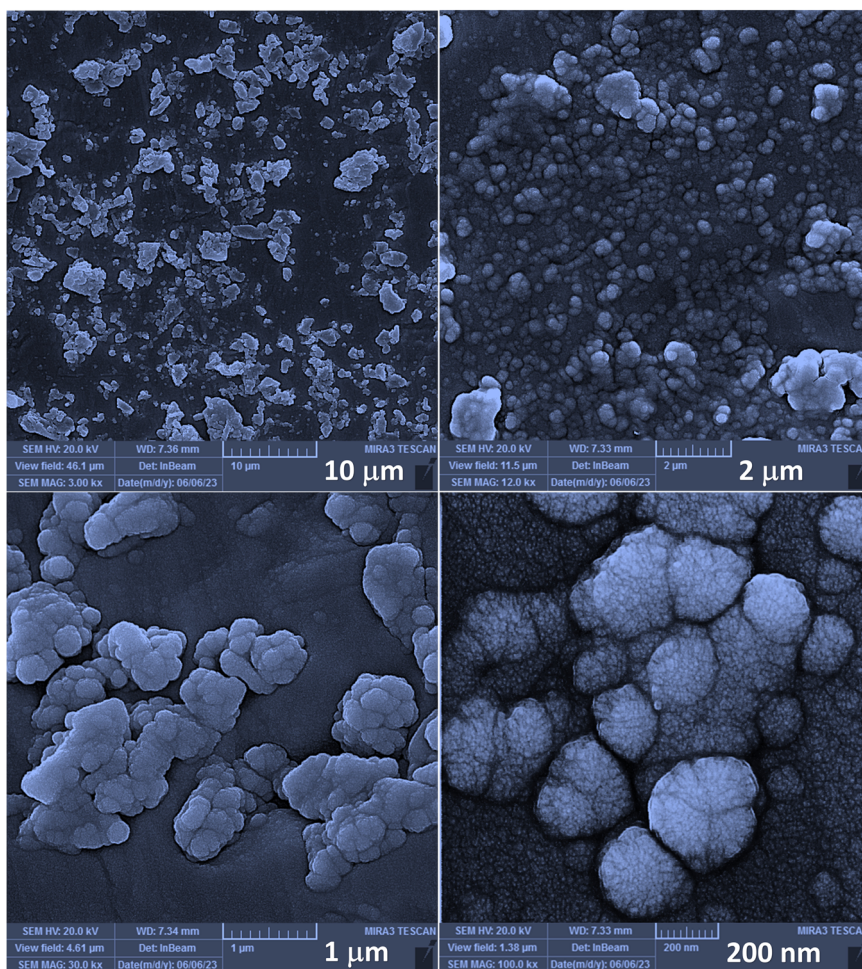
comparison. The PSD of investigated BCFH-SBA-15 reveals that the material has two general distributions of micropores and mesopores with APD of 2 nm and 4 nm, respectively, as shown in Fig. 2d. Here, we suggest that the presence of the micropores within the BCFH-SBA-15 structure can be attributed to the attachment of SCA-bearing cyclam molecules into the mesopores during surface modification and the formation of the silica layers around the meso-sized hexagonal arrays of the organic template and the reduction of the diameter of the mesopores. It should also be noted that it has been reported that SBA-15 naturally has micropores within walls[43]. The simultaneous presence of micropores and mesopores in the NSPs, such as BCFH-SBA-15, presents a promising advantage that can improve the penetration phenomenon, reduce the rate of blockage of pores and channels, and subsequently amplify the efficiency of the material for being used in applications such as adsorption, extraction, catalysis, and drug delivery[40,44,45].

Figure 3 FESEM images of the BCFH-SBA-15 at four different magnifications (3000x, 12,000x, 30,000x, and 100,000x) clearly show particles with a homogeneous spherical morphology and almost uniform particle size ranging from 150 to 500 nm. The homogeneity and consistent quality of the particles as well as the lack of impurities, which usually manifest in varying sizes and shapes alongside the synthesized nanoparticles, indicate the high purity of the silica source utilized in producing the substance. This assertion can also be validated through FESEM-mapping analysis. The uniform distribution of the constituent elements of the material, namely silicon, oxygen, carbon, and nitrogen on the surface of the material is readily discernible as shown in Fig. 4, confirming the even distribution of the SCAs-bearing cyclam on the surface and the successful completion of the one-pot surface modification procedure.

The utilization of the TEM technique was imperative to visually authenticate the porous structure of the material. As demonstrated in Fig. 5, the BCFH-SBA-15 material is comprised of well-ordered micro-meso cavity channels arranged in parallel rows. The exceptional consistency and conformity of the channels are indicative of the triumphant synthesis route and highly pure silica source. This structure bears resemblance to previously documented structures, which utilized tetra-n-alkoxysilane (such as TMOS, TEOS, etc.) as laboratory silica sources for the synthesis of SBA-15 with long-range ordered mesopores[37,46].

Adsorption studies

Following the synthesis and structural characterization of the BCFH-SBA-15, adsorption studies were conducted to evaluate its removal performance toward Ni(II) from aqueous solutions. The adsorption process was systematically monitored by examining the impact of influential adsorption parameters such as W (g), pH, T (K), C_i (mg g^{-1}), and t (min). Various isotherm, thermodynamic, and kinetic equations were utilized to investigate the adsorption mechanisms and the functionality of the adsorbent. A comprehensive list of the adsorption equations and parameters implemented in this study is provided in Table 1. To ensure accurate analysis of isotherm and kinetic data, the nonlinear forms of the equations were employed, which exhibit a higher accuracy coefficient and substantially lower error compared to linear equations[47–51]. Furthermore, the thermodynamic data derived from adsorption isotherms were obtained using the most recent correction methods published in recent literature. Subsequently, the data extrapolated from these equations will be thoroughly examined in the following sections.
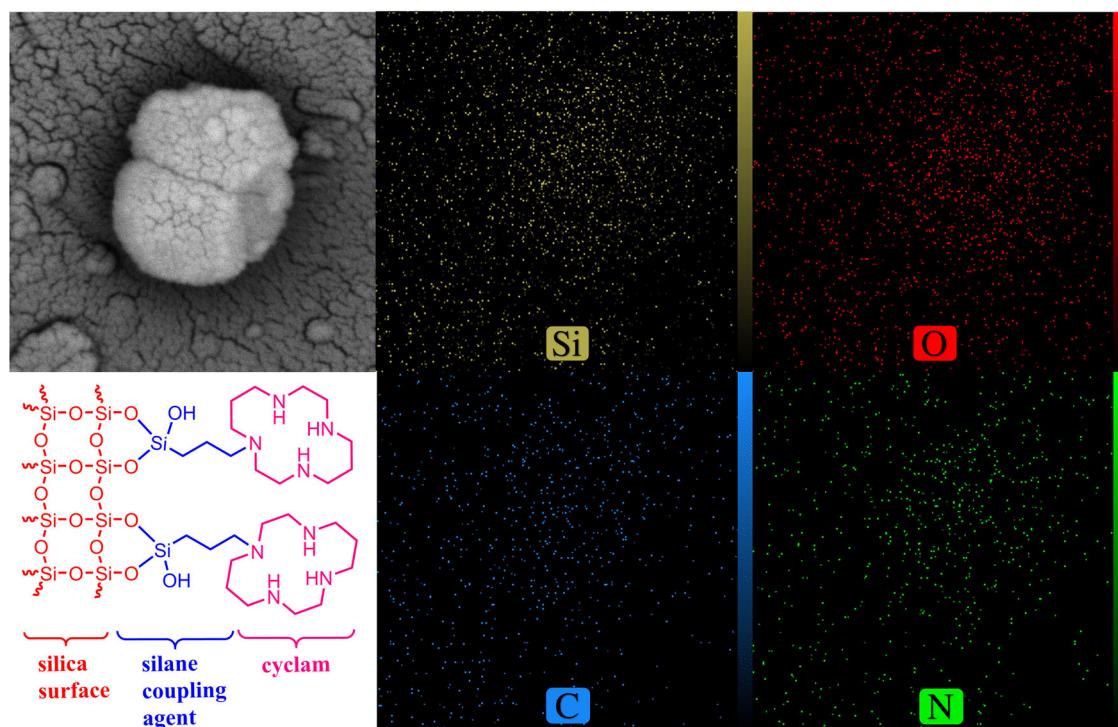
Fig. 4 | FESEM-mapping images of the adsorbent. FESEM-mapping images of BCFH-SBA-15 along with showing the schematic structure of the material containing the main constituent elements.
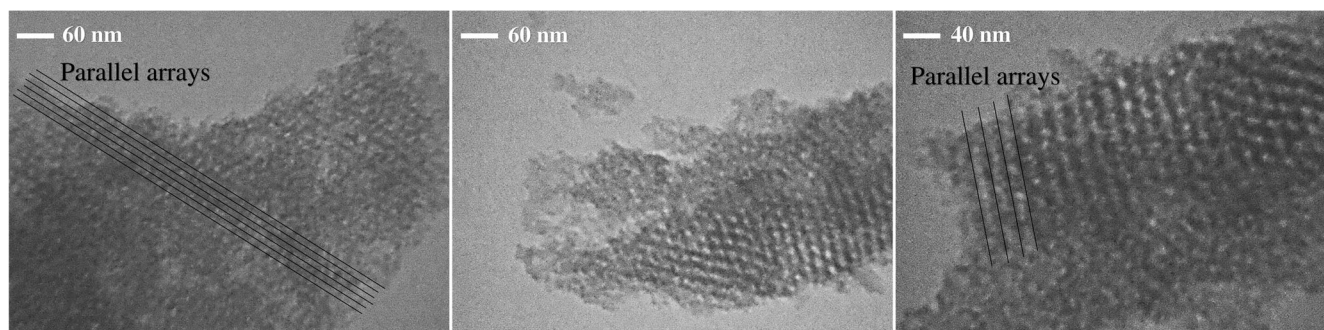

Fig. 5 | TEM micrographs. TEM images of BCFH-SBA-15 (length of scale bars, from left to right = 60 nm, 60 nm, 40 nm).

The effect of pH and adsorbent dose

The parameter of pH is widely recognized as a crucial factor in the process of adsorption, as it has the capability to influence the adsorption intensity through alterations in the physical and chemical characteristics of both the adsorbent and the adsorption medium. Given that the quantity of this variable differs between natural and industrial water settings, it is imperative to diligently track the transformations in adsorption levels corresponding to pH fluctuations, to accurately simulate the adsorption process in such environments. The quantity of adsorbent dosage is a crucial economic factor within the absorption process, primarily due to the direct correlation between the amount of adsorbent employed and production costs. As a result, less adsorbent usage can lead to a decrease in production costs. Additionally, the quantity of secondary pollution and the expenses associated with separating the process of adsorbent can be reduced based on the amount of adsorbent utilized. Therefore, in this work, the simultaneous effect of pH and the amount of adsorbent on the adsorption performance under constant conditions (C_i = 10 mg L^{-1}, V = 20 mL, t = 60 min, T = 298 K, RPM = 180) was investigated. The outcomes displayed in Fig. 6(a) demonstrate that as pH increased from 3.0 to 6.0, the adsorption capacity increased for all levels of adsorbent. However, as the pH increased further to 7.0, there was no considerable shift in the adsorption capacity, and it remained almost constant (only a slight decrease in adsorption capacity was observed). Nevertheless, the adsorption capacity displayed a descending trend in the subsequent stages as pH increased beyond 7.0. Also, in all investigated pHs, with the increasing amount of adsorbent from 1.00 to 3.00 mg, the amount of adsorption capacity increased with an almost constant rate, but with a further increase of adsorbent dose up to 4.00 mg, this ascending slope decreased and no significant increase in the adsorption capacity was observed. Accordingly, pH = 6.0 and W = 3.00 mg were selected as optimum values for pH and adsorbent dose for further studies. W

The effect of initial concentration and temperature (isotherm and thermodynamic studies)

In order to investigate the isotherms of Ni(II) adsorption on BCFH-SBA-15, the amount of changes in Q_e (mg g^{-1}) values were investigated by increasing the C_i C_i (mg L^{-1}) values from 1 to 200 mg L^{-1} at four different temperatures (298, 303, 308, and 313 K) under constant conditions (pH = 6.0, W = 3.00 mg, V = 20 mL, t = 60 min, RPM = 180). It is of significance to highlight that recent studies strongly recommend that the most optimal and precise approach to investigate the thermodynamic data of an adsorption

Table 1 | Adsorption equations and different theoretical models used in this study

Name/Model	Equations	Refs.
General equilibrium aquations		
(1) Removal percentage (%)	$\%R = (C_i - C_e) \times 100/C_i$	16
(2) Adsorption capacity at time t	$Q_t = (C_i - C_t) \times (W/V)$	16
(3) Adsorption capacity at equilibrium	$Q_e = (C_i - C_e) \times (W/V)$	16
Isotherm Models		
(4) Langmuir	$Q_e = (Q_m, \mathrm{cal.} \bullet K_L \bullet C_e)/(1 + K_L \bullet C_e)$	54,86
(5) Freundlich	$Q_e = (K_F \bullet C_e^{1/n})$	55
(6) Redlich-Peterson	$Q_e = (K_{RP} \bullet C_e)/(1 + \alpha_{RP} \bullet C_e^{g_{RP}})$	56
Thermodynamic Equations		
(7) Thermodynamic equilibrium constant	$K_e^\circ = (1000 \bullet K_L \bullet M_w) \times [adsorbate]^\circ/\gamma$	52
(8) Van 't Hoff equation	$\mathrm{Ln}K_e^\circ = -\left(\triangle H_{ads.}^\circ/R \bullet T\right) + (\triangle S_{ads.}^\circ/R)$	61
(9) Gibbs Free Energy	$\triangle G_{ads.}^\circ = \triangle H_{ads.}^\circ - T \bullet \triangle S_{ads.}^\circ$	61
Kinetic Models		
(10) PFO	$Q_t = Q_{e,cal.} \bullet (1 - e^{-k_1 \bullet t})$	69
(11) PSO	$Q_t = (Q_{e,cal.}^2 k_2 \bullet t)/(1 + Q_{e,cal.} k_2 \bullet t)$	87
(12) Elovich	$Q_t = (1/\beta)\ln(\alpha \bullet \beta) \bullet t$	88
(13) IPD	$Q_t = k_{diff.} \bullet t^{1/2} + C$	89

process is to utilize a nonlinear form of isotherm models, such as the Langmuir model, at varying temperatures[52,53]. So, at first, the effect of the initial concentration of nickel on Q_e (mg g^{-1}) values at a constant temperature was investigated, and then different isotherm equations, *viz.* Langmuir[54], Freundlich[55], and R-P[56], were fitted to the experimental data to select the best isothermal adsorption behavior, and then isothermal parameters at four different temperatures were used in order to extrapolate thermodynamic parameters including $H_{ads.}^\circ$ (kJ mol^{-1}), $S_{ads.}^\circ$ (kJ mol^{-1} K^{-1}), and $G_{ads.}^\circ$ (kJ mol^{-1}).

Figure 6(b) illustrates the alterations in the Q_e values against the increase in the C_e (mg L^{-1}) values of nickel (where each C_e value corresponds to a particular C_i value). C_e denotes the quantity of concentration left in the solution and in the state of equilibrium, which was not adsorbed on the surface of the absorbent. As depicted in Fig. 6b, an increase in the C_i values (and therefore C_e values) from 1 to 20 mg L^{-1} leads to a sharp rise in the Q_e values, followed by a decrease in slope within the C_i range of 20 to 50 mg L^{-1}, and ultimately Q_e values reached a plateau in the range of 50 to 200 mg L^{-1}. The same trend was observed in all four applied temperatures employed in the study. Notably, the $Q_{m,exp.}$ values recorded at temperatures of 298, 303, 308, and 313 K were 240.00, 253.33, 263.33, and 270.67 mg g^{-1}, respectively. Also, with the increase in temperature, the adsorption rate increased, which probably indicates the positive effect of temperature in increasing the activity of the adsorbent and the affinity of Ni(II) cations to the surface functional groups (active adsorption sites) of the adsorbent. However, the increasing trend of Q_e values with increasing temperature is characterized by the following trend: $(T = 298\,\mathrm{K} \rightarrow T = 303\,\mathrm{K}) > (T = 303\,\mathrm{K} \rightarrow T = 308\,\mathrm{K}) > (T = 308\,\mathrm{K} \rightarrow T = 313\,\mathrm{K})$. The aforementioned trend illustrates that augmenting the temperature to levels surpassing 313 K may not manifest a noteworthy augmentation like the upsurge witnessed in lower temperature intervals.

To gain a better insight into the adsorption behavior of Ni(II) on BCFH-SBA-15, the nonlinear form of the Langmuir (Fig. 6(c)), the Freundlich (Fig. 6(d)), and the R-P (Fig. 6(e)) isotherm equations were fitted to the obtained experimental data. The numerical values of the isotherm parameters of these equations were calculated by the nonlinear curve fitting method and their values are listed in Table 2.

By comparing between Langmuir and Freundlich two-parameter models, it can be seen that the Langmuir model shows a better fit to the experimental data at four temperatures (based on $R_{Adj.}^2$ values). Furthermore, the results obtained from the Langmuir model reveal a significant level of concordance between the calculated values of maximum adsorption capacities ($Q_{m,cal.} = 243.36$, 253.87, 260.97, and 266.28 mg g^{-1}) and experimentally obtained values of maximum adsorption capacities ($Q_{m,exp.} = 240.00$, 253.33, 263.33, and 270.67 mg g^{-1}) at all four temperatures. This is indicative of the superior efficacy of the Langmuir model over the Freundlich model in characterizing the adsorption characteristics of Ni(II) on the BCFH-SBA-15. In instances where a comparison between the Langmuir and the Freundlich models is necessary, one can utilize the R-P three-parameter equation and assess the g parameter's numerical value. In the R-P model (Eq. (6)), the reduction of g_{RP} parameter to one results in the transformation of the R-P model into the Langmuir equation. In doing so, it can be inferred that the closer the value of g_{RP} is to unity, the adsorption behavior will demonstrate similarity to the Langmuir equation, and the closer this parameter is to zero, the more consistent the model is with the Freundlich model[57,58]. By calculating the values obtained for the g_{RP} parameter, as given in Table 2, in the Ni(II) adsorption process at all four assessed temperatures ($g_{RP} = 0.9905$, 0.9198, 0.9584, and 0.9436 at 298, 303, 308, and 313 K), it can be concluded that their proximity to one is an additional confirmation that the Langmuir model shows a better fit to the experimental data than the Freundlich model. Accordingly, the adsorption of Ni(II) on the surface of the adsorbent is homogeneous (monolayer adsorption), where the adsorbed layer consists of a single molecule in thickness. Also, Ni(II) adsorption is limited to a finite and fixed number of definite localized sites (cyclam groups) that are identical and equivalent in nature. Furthermore, there is no lateral interaction and steric hindrance present between the Ni(II) ions in the solution, even when situated on adjacent sites all cyclam-adsorptive sites possess equal affinity toward the Ni(II)[51,59].

Thermodynamic investigations of Ni(II) adsorption on the BCFH-SBA-15 were carried out in order to gain further insights into the nature of the adsorption process from the point of view of energy and the spontaneity of the process. Leveraging the outcomes of earlier findings on the optimal approach to compute the thermodynamic data of adsorption, the thermodynamic formulae given in Table 1 were employed to estimate the numerical values of K_e°, $\triangle H_{ads.}^\circ$, $\triangle S_{ads.}^\circ$, and $\triangle G_{ads.}^\circ$[60,61]. Numerical values of $\triangle H_{ads.}^\circ$ and $\triangle S_{ads.}^\circ$ can be obtained from Van 't Hoff equation (Eq. (7))—by constructing a linear plot of $\ln K_e^\circ$ versus $1/T$, in which the changes in entropy and enthalpy can be calculated from the intercept and the slope, respectively. The values of $\triangle G_{ads.}^\circ$ at a given temperature can easily be calculated from Eq. (9). However, to determine the equilibrium constant (K_e°) for an adsorption system, it is essential to acquire isotherms of adsorption at varied temperatures through a proper methodology by using a nonlinear curve fitting of isotherm data. In order to effectively apply Vant Hoff's equation, the K_e° parameter must be dimensionless. Therefore, the K_L (L mg^{-1}) constant is typically employed in Vant Hoff's equation. By plotting adsorption isotherms at four distinct temperatures (Fig. 6(b)), and nonlinear fitting of the Langmuir equation (Fig. 6(c)) for all given temperatures, four numerical values are obtained for the K_L parameter at a given temperature. Subsequently, four different values for K_e° are obtained by inserting the K_L values into the Van Hoff equation. Finally, a linear graph is constructed by plotting $\ln K_e^\circ$ versus $1/T$ as depicted in Fig. 6(f).

The calculated thermodynamic values are given in Table 3. The values of $\triangle H_{ads.}^\circ$ and $\triangle S_{ads.}^\circ$ for adsorption of Ni(II) cations on BCFH-SBA-15 were calculated to be 122.61 kJ mol^{-1} and 0.5093 kJ mol^{-1} K^{-1}. The numerical values of $\triangle G_{ads.}^\circ$ at 298, 302, 308, and 313 K were calculated to be −29.161, −31.708, −34.254, and −36.801 kJ mol^{-1}, respectively, indicating that increasing temperature has a positive impact on the adsorption process. Also, the negative values of $\triangle G_{ads.}^\circ$ demonstrated that the adsorption possesses a spontaneous nature[62]. The elucidation of the positive $\triangle H_{ads.}^\circ$ value is indicative of the endothermic character of the adsorption. Moreover, the positive value of $\triangle S_{ads.}^\circ$ corroborates that the degree of randomness increases at the interface of the solid-solution during the adsorption process.
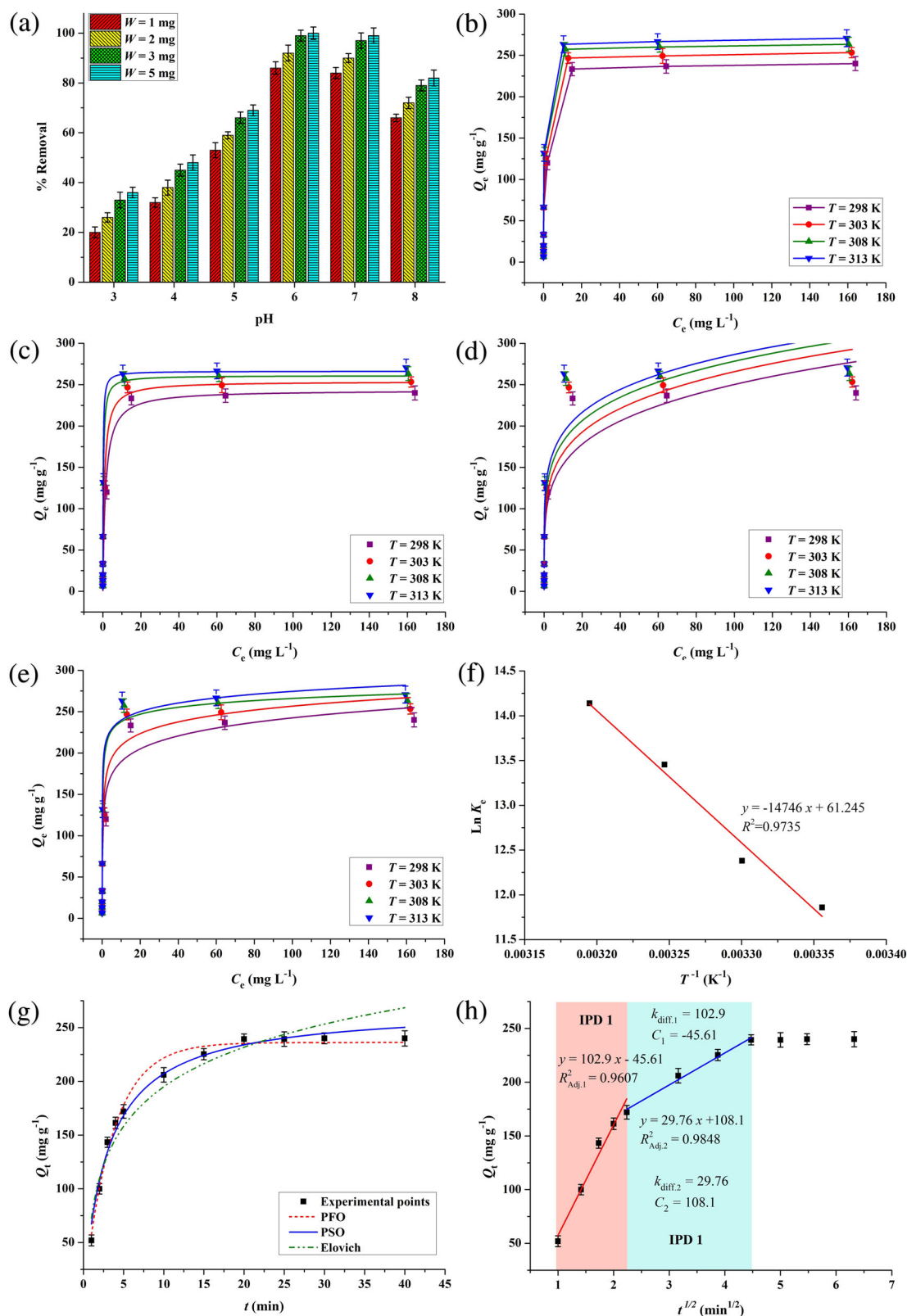
Fig. 6 | Optimization and fitting studies for adsorption of Ni(II) using BCFH-SBA-15. Simultaneous effect of pH and adsorbent dose on Ni(II) removal percentage (**a**); the effect of changes in C_e values on Q_e values at four different temperatures (**b**); isotherm curves fitted to experimental data according to the nonlinear forms of the Langmuir (**c**), the Freundlich (**d**), and R-P models at different temperatures (**e**); linear diagram of LnK_e° versus $1/T$ (**f**); the effect of contact time on Q_t and different kinetic models fitted to the experimental data (**g**); linear diagram of IPD kinetic model fitted to the experimental data (**h**).

The low value of $\triangle S^{\circ}_{ads.}$ may suggest that there was no notable alteration in entropy that transpired during the process of Ni(II) adsorption by BCFH-SBA-15.

Previous reports have demonstrated that the numerical value of the $\triangle H^{\circ}_{ads.}$ (kJ mol^{-1}) and $\triangle G^{\circ}_{ads.}$ (kJ mol^{-1}) parameters are indicative of the type of interaction between the adsorbent and the adsorbate. In this regard, the type of interaction can be placed in one of the following categories: chemical adsorption $(-400 < \triangle G^{\circ}_{ads.} < -80$ or $\triangle H^{\circ}_{ads.} > 60)$, physical adsorption $(-20 < \triangle G^{\circ}_{ads.} < 0$ or $\triangle H^{\circ}_{ads.} < 40)$, exchange of dentate $(\triangle H^{\circ}_{ads.} \approx 40)$, hydrogen bonding forces $(2 < \triangle H^{\circ}_{ads.} < 40)$, dipole-dipole interaction $(2 < \triangle H^{\circ}_{ads.} < 29)$, and van der Waals forces $(4 < \triangle H^{\circ}_{ads.} < 10)$[57,63,64]. According to this instruction and based on calculated values of $\triangle H^{\circ}_{ads.} = 122.61$ kJ mol^{-1} and $\triangle G^{\circ}_{ads.} = -29.161$ to -36.801 kJ mol^{-1}, the adsorption of Ni(II) on BCFH-SBA-15 is in the range of chemical adsorption. This shows that the interaction between Ni(II) cations and cyclam functional groups on the surface of the adsorbent in an aqueous solution is strong.

The high strength of the bond between the central Ni(II) metal in a + 2 oxidation state and the nitrogen groups in the cyclam ring (C-N) forms a very strong and stable tetra-N-substituted complex. This claim is based on the thermodynamic findings (strong chemical adsorption) of this research and previous studies regarding the binding energy of Ni(II) in a C-N complex confirmed by instrumental analyses and kinetic investigations[65–68]. Considering that the catalytic properties of nickel have been previously confirmed, particularly when coordinated with the cyclam ring with a + 2 oxidation state[65], its complex can be used as a catalyst after adsorbing Ni(II) by BCFH-SBA-15. The prospect of using BCFH-SBA-15 as a catalyst can be drawn in the continuation of its use as an adsorbent, which is beyond the scope of this article and should be addressed in the future.

The effect of contact time and kinetic studies

Contact time is regarded as a significant aspect of the adsorption procedure, serving as a utilitarian factor in the assessment of the efficacy of adsorbents. Hence, the adsorbent can be deemed more economically and operationally efficient when the adsorption time is decreased. As can be seen from Fig. 6g, the changes in adsorption capacity were tested within a 40-min duration under constant conditions $(C_i = 200$ mg L^{-1}, $W = 3.00$ mg, $V = 20$ mL, $T = 298$ K, RPM = 180), and it was observed that the adsorption profile includes three general stages: with the initial 4 min being characterized by an intense increase in absorption, followed by a decrease in slope between minutes 5 and 15, while the absorption rate remains elevated. After 20 min, the adsorption reached equilibrium and no change occurred in the adsorption capacity of the adsorbent.

In order to investigate the kinetics of Ni(II) adsorption on the BCFH-SBA-15, three prevalent nonlinear models, namely PFO (Eq. (10))[69], PSO (Eq. (11))[70], and Elovich (Eq. (12))[71], along with the linear model of IPD (Eq. (13)) were used, and after fitting them to the experimental data, the numerical values of the corresponding parameters are listed in Table 4.

In order to find the best-fitted kinetic model, it is essential to consider the kinetic equation that exhibits the least deviation between the theoretical (calculated) adsorption capacity $(Q_{e,cal.})$ and the experimental adsorption capacity $(Q_{e,exp.})$, while also demonstrating the highest $R^2_{Adj.}$. This model is deemed optimal for describing the kinetic suitable for the adsorption process. Upon analysis, it has been determined that PFO $(Q_{e,cal.} = 236.18$ mg g^{-1}, $R^2_{Adj.} = 0.9886)$ and PSO $(Q_{e,cal.} = 268.99$ mg g^{-1}, $R^2_{Adj.} = 0.9841)$ models exhibit a superior level of fitting compared to the Elovich $(\alpha = 208.6$ mg g^{-1} min^{-1}, $R^2_{Adj.} = 0.9473)$ model to the experimental data $(Q_{e,exp.} = 240.00$ mg g$^{-1})$. Nevertheless, when comparing the two models, it is apparent that the PFO model displays a slightly greater degree of agreement than the PSO model. This implies that the kinetics of nickel adsorption on the BCFH-SBA-15 is a result of a combination of both PFO and PSO models but with a greater percentage of participation from the PFO model.

In order to investigate the number of adsorption steps involved in the Ni(II) adsorption process, the IPD kinetic model was used. As shown in Fig. 6(h), Ni(II) adsorption follows two main stages before reaching maximum adsorption at equilibrium at 20 min.

1. The primary phase (IPD1) occurs within a range of 1 to 4 min and corresponds to the surface covering of metal ions.
2. The second phase of the process, referred to as IPD2, occurs throughout 5 to 15 min and is associated with the diffusion of ions into the bimodal micro-mesoporous structure. The hydrated ionic radius of Ni has been determined to be 0.404 nm[72], a value significantly smaller than the average pore size of the BCFH-SBA-15 material. This suggests that the adsorption process is not hindered by size exclusion effects. Furthermore, the presence of numerous micropores affords a greater internal space for the diffusion of heavy metal species.

Adsorption mechanism and removal behavior of Ni(II) on the adsorbent

Based on our experimental findings, we can elucidate the mechanism of Ni(II) uptake by the adsorbent as follows:

Cyclam groups. The adsorption of Ni(II) by the adsorbent involves the interaction between Ni(II) ions and the cyclam groups present on the adsorbent surface. Cyclam groups are known for their strong metal-binding capability, and they form coordination complexes

Table 2 | The values of isotherm models' parameters at different temperatures

Isotherm model	T	298 K	303 K	308 K	313 K
	$Q_{m,exp.}$	240.00	253.33	263.33	270.67
Langmuir	$Q_{m,cal.}$	243.36	253.87	260.95	266.28
	K_L	0.6921	1.1650	3.4095	6.7618
	$R^2_{Adj.}$	0.9448	0.9639	0.9828	0.9778
Freundlich	n	4.718	4.994	5.379	5.737
	K_F	94.28	105.67	118.23	128.38
	$R^2_{Adj.}$	0.8837	0.8878	0.8773	0.8808
Redlich-Peterson	α_{RP}	6.085	5.130	5.904	17.25
	K_{RP}	935.89	912.73	1299.6	3657.3
	g_{RP}	0.9905	0.9198	0.9584	0.9436
	$R^2_{Adj.}$	0.9583	0.9673	0.9839	0.9830

Table 3 | The values of thermodynamic parameters

$\triangle H^{\circ}_{ads.}$	$\triangle S^{\circ}_{ads.}$	$\triangle G^{\circ}_{ads.}$			
		298 K	303 K	308 K	313 K
122.61	0.5093	−29.161	−31.708	−34.254	−36.801

Table 4 | The values of kinetic models' parameters at 298 K

$Q_{e,exp.}$	PFO			PSO			Elovich		
	k_1	$Q_{e,cal.}$	$R^2_{Adj.}$	k_2	$Q_{e,cal.}$	$R^2_{Adj.}$	α	β	$R^2_{Adj.}$
240.00	0.2795	236.18	0.9886	0.0012	268.99	0.9841	208.6	0.018	0.9473

Table 5 | Comparison table between Ni(II) adsorption capacities on different reported adsorbents along with important adsorption parameters involved in the adsorption process

Adsorbent	$Q_{m.exp.}$ (mg g^{-1})	$Q_{m.cal.}$ (mg g^{-1})	pH	W (g L^{-1})	T (K)	t(min)	year	Refs.
BCFH-SBA-15	270.67	266.28	6.0	0.15	313	20	2024	This work
	263.33	260.95	6.0	0.15	308	20		
	253.33	253.87	6.0	0.15	303	20		
	240.00	243.36	6.0	0.15	298	20		
MWCNTs-KIAgNPs	164.26	174.78	6.0	0.4	318	60	2021	76
MPB	-	155	7.0	1	298	60	2019	77
SiO$_2$-(2)	-	111.7	5.4	1	RT	1440	2020	78
NH$_2$-SBA-15	-	90.1	5.0	1	333	60	2020	79
Ni(II)-IIP	-	86.3	7.0	-	298	30	2018	80
Coirpith carbon	64.38	62.5	5.0	0.6	303	40	2001	81
HO-Fe$_3$O$_4$@SiO$_2$-AP	-	57.52	6.0	-	298	260	2021	82
HE-Fe$_3$O$_4$@SiO$_2$-AP	-	45.19	6.0	-	298	260		
SA-2	-	49.75	7.0	2	318	480	2019	83
EDSG	19.3	18.3	3.0	2	RT	3000	2011	84
DTSG	20.4	17.5	3.0	2	RT			
HLS	15.7	15.92	5.0	10	303	1440	2007	85

with Ni(II) ions. This coordination interaction between the cyclam groups and Ni(II) contributes significantly to the adsorption process.

Silanols. In addition to the cyclam groups, the silanol groups present on the mesoporous silica surface of the adsorbent also play a role in Ni(II) uptake. Silanol groups contain hydroxyl (-OH) functional groups, which can participate in electrostatic interactions with metal ions, including Ni(II). These interactions further contribute to the adsorption of Ni(II) on the adsorbent surface.

pH influence. Our studies have shown that a pH range of 6.0 to 7.0 is most suitable for achieving maximum adsorption of Ni(II). This pH range is likely favorable for the formation of coordination complexes between Ni(II) ions and the cyclam groups, as well as for optimizing the electrostatic interactions between Ni(II) and the silanol groups.

Isotherm and kinetic behavior. The adsorption isotherm analysis indicated that the adsorption of Ni(II) by our adsorbent mostly followed the Langmuir isotherm, suggesting monolayer adsorption with a finite number of active sites. Additionally, the adsorption kinetics could be described by both the PFO and PSO models, indicating that the adsorption process involves both surface adsorption and chemisorption mechanisms.

Intraparticle diffusion. The IPD model revealed that the adsorption process consists of two phases. The initial phase corresponds to the surface coverage of metal ions, where Ni(II) ions rapidly attach to the available active sites on the adsorbent surface. The subsequent phase involves the diffusion of Ni(II) ions into the pores of the adsorbent, allowing for further adsorption.

Enthalpy change ($\triangle H_{ads.}^{\circ}$). The value of $\triangle H_{ads.}^{\circ}$ was determined to be 122.61 kJ mol^{-1}. This positive value indicates that the adsorption of Ni(II) onto our adsorbent involves a strong chemisorption process. The positive $\triangle H_{ads.}^{\circ}$ suggests an endothermic nature of the adsorption, indicating that energy is required to break existing bonds and establish new bonds between Ni(II) ions and the adsorbent surface.

Gibbs free energy change ($\triangle G_{ads.}^{\circ}$). The values of $\triangle G_{ads.}^{\circ}$ were calculated to be in the range of -29.161 to -38.801 kJ mol^{-1}. The negative values of $\triangle G_{ads.}^{\circ}$ indicate that the adsorption of Ni(II) onto our adsorbent is a spontaneous process. The more negative the $\triangle G_{ads.}^{\circ}$ value, the more favorable and spontaneous the adsorption becomes. Therefore, the negative values obtained in our study suggest that the adsorption of Ni(II) onto our adsorbent is energetically favorable.

Entropy change ($\triangle S_{ads.}^{\circ}$). The value of $\triangle S_{ads.}^{\circ}$ was found to be 0.5093, indicating a low degree of randomness during the adsorption process. A positive value of $\triangle S_{ads.}^{\circ}$ would suggest an increase in randomness during adsorption, whereas a negative value would indicate a decrease in randomness. In our case, the positive value of $\triangle S_{ads.}^{\circ}$ suggests a slight increase in randomness during the adsorption process.

Comparison study

Table 5 shows a comparative study to show different adsorbents for the adsorption of Ni(II), which includes the comparison of various parameters such as adsorption capacity, pH, adsorbent dose, temperature, and adsorption time.

According to a comparative analysis between BCFH-SBA-15 and various adsorbents reported between 2001 to 2021, the BCFH-SBA-15 synthesized in this study demonstrated the highest level of Ni(II) adsorption capacity as well as the shortest adsorption time. The outcomes suggest that BCFH-SBA-15 exhibits a remarkable level of excellence when compared to other adsorbents, which exhibit the subsequent characteristics:

- The highest adsorption capacity: Firstly, the bimodal micro-mesoporous structure of the BCFH-SBA-15 provides exceptional intraparticle diffusion pathways, leading to a heightened degree of accessibility to the adsorption sites. Secondly, the high surface area of the BCFH-SBA-15 (325 m^2 g^{-1}) is directly proportional to the increase in the number of adsorption sites (cyclam groups) and the contact of the adsorbent surface with the solution containing adsorbate. Finally, the presence of abundant and uniform distributed cyclam adsorption sites on the BCFH-SBA-15 surface with a strong propensity to adsorb Ni(II) cations also contributes to the superior adsorption capacity.
- The shortest adsorption time: the above reason can be considered one of the main reasons for the excellent adsorption kinetics of the BCFH-SBA-15 (t = 20 min), leading to a reduced adsorption time.
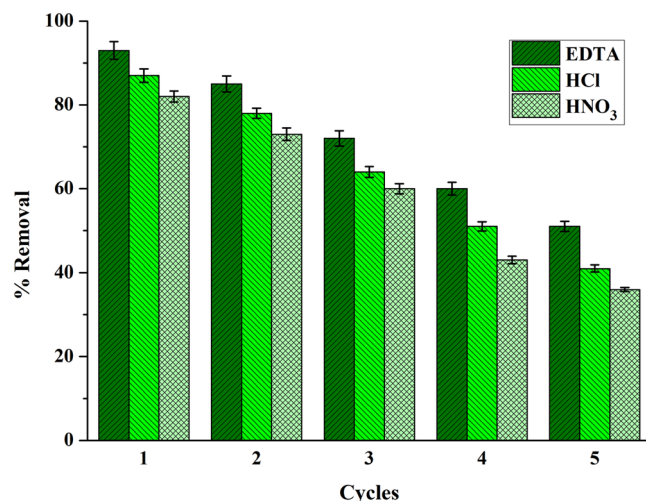- The cost-effective and ecologically sustainable production of

Fig. 7 | Regeneration performance of BCFH-SBA-15. The regeneration performance of the saturated BCFH-SBA-15 adsorbent after 5 consecutive cycles in EDTA, HCL, and HNO₃ as cost-effective eluents.

BCFH-SBA-15: this is attributed to the biological origin of silica (derived from sorghum agricultural waste) and its use as an inexpensive and ubiquitous source of silica for the production of NSPs.
- Biodegradability: NSPs possess a notable benefit owing to their non-toxic and biodegradable structure, which renders them environmentally friendly. This biodegradable nature is a crucial feature in the realm of sustainable materials, and it provides a distinct advantage over other alternatives.

Regeneration study

The ability to reuse adsorbents is a crucial factor in determining their effectiveness. In this study, the stability and regenerative capability of BCFH-SBA-15 as an adsorbent were meticulously evaluated through a total of five consecutive adsorption/desorption cycles under optimal conditions obtained in the previous sections. To extract the previously loaded Ni(II) ions, three cost-effective reagents, including HCl (0.01 mol L⁻¹), EDTA (0.01 mol L⁻¹), and HNO₃ (0.01 mol L⁻¹) were evaluated. In this specified concentration, i.e., 0.01 mol L⁻¹, it has been reported that these eluents do not inflict any damage or alteration to the chemical composition of a silica-based absorbent[73]. After the adsorption process, the BCFH-SBA-15 underwent multiple washes utilizing DDW and was subsequently rinsed with the eluent. Following this, the BCFH-SBA-15 was subjected to a vacuum oven-drying process at a temperature of 333 K for a duration of 10 h. Finally, the adsorbent was reused under the same conditions for the subsequent run. As indicated in Fig. 7, EDTA proved to be the best eluent for the desorption of Ni(II) ions from the adsorbent. As depicted in Fig. 7, it is evident that the efficacy of the BCFH-SBA-15 adsorbent for Ni(II) removal experiences a consistent decline with a continuous increase in the number of recycling cycles. Moreover, the order of effectiveness of acids in the recycling procedure is found to be EDTA>HCl>HNO₃. Although utilizing HCl and HNO₃ eluents may be more cost-effective compared to EDTA eluent, the desorption data gathered suggests that the efficacy of EDTA for the desorption of Ni(II) in the regeneration process is marginally superior to that of HCl. This observation can be ascribed to the creation of a strong chelating between EDTA and Ni ions[74]. In the case of EDTA, the removal percentage underwent a marked decrease from approximately 93% in the initial round to roughly 51% in the fifth round. It is noteworthy, however, that in the third round, the value still held a considerable magnitude of 72%.

This observation can be attributed to the profound affinity of cyclam groups to retain nickel ions in the form of a strong cyclam-Ni(II), as substantiated by thermodynamic data, within the absorptive structure. The outcome of this phenomenon is conspicuously reflected in the efficiency of

the desorption process. Based on these observations, it is suggested that the adsorption of Ni(II) ions, in the form of cyclam-Ni(II) complexes, by the BCFH-SBA-15 effectively transforms the BCFH-SBA-15 adsorbent into a highly suitable substrate for a Ni-based catalyst that can be utilized in the investigation of catalytic reactions. This intriguing notion warrants further investigation, either by ourselves or by other interested parties in the future.

Conclusion

In this article, we discussed the synthesis of a biogenic cyclam-functionalized homologous SBA-15 (BCFH-SBA-15) as a step towards sustainable and eco-friendly production methods for nanomaterials and their use in environmental applications. The preparation of BCFH-SBA-15 involved the utilization of agricultural waste from sorghum, a commonly consumed crop, as a source of silica. The resultant material exhibited a bimodal micro-mesoporous structure and a significant surface area of $325 \, m^2 \, g^{-1}$, all achieved through a simple one-pot environmentally friendly process. Structural characterization of BCFH-SBA-15 was carried out using a range of instrumental analyses including XRD, FTIR, FESEM, TEM, and nitrogen adsorption/desorption isotherms. The material was found to be highly effective in adsorbing Ni(II) in aqueous solutions, with the best fit to the experimental data being obtained using the Langmuir isotherm model. The maximum adsorption capacity of BCFH-SBA-15 in optimal conditions (pH = 6.0, adsorbent dose = 3.00 mg, contact time = 20 min) and at four different temperatures (298, 303, 308, and 313 K) was calculated to be 243.36, 253.87, 260.95, and 266.28 mg g⁻¹, respectively, which is better than most previously reported adsorbents for Ni(II) removal. Thermodynamic data indicated that Ni(II) adsorption on BCFH-SBA-15 was a strong chemisorption process ($\triangle H^{\circ}_{ads.} = +122.61 \, kJ \, mol^{-1}$) that was spontaneous ($\triangle G^{\circ}_{ads.} = -29.161$ to $-36.801 \, kJ \, mol^{-1}$) with a low degree of randomness ($\triangle S^{\circ}_{ads.} = +0.5093 \, kJ \, mol^{-1}$). This study provides evidence that the utilization of agricultural waste for the synthesis of nanomaterials can be a sustainable and efficient approach towards environmental remediation and BCFH-SBA-15 can function as a potent adsorbent for the adsorption of Ni(II). Furthermore, it is recommended that the investigation of the post-adsorption characteristics of BCFH-SBA-15 as a catalyst be explored in subsequent research endeavors, as a result of the existence of cyclam-Ni(II) complexes within the catalyst's porous structure. Such studies may be pursued by ourselves or other scholars in the future.

Methods
Chemicals
P123 (PEG20-PPG70-PEG20, average Mn ~5800), 1,4,8,11-tetra-azacyclotetradecane (cyclam, 98%), 3-IPTMS (≥95%), Ni(NO₃)₂·6H₂O (≥99%), EDTA (≥99%), and anhydrous Na₂CO₃ (≥99%) were purchased from Sigma-Aldrich (Germany). Acetonitrile (≥ 99.9%), ethanol, pentane (>98%), NaOH (pellets, ≥97%), HNO₃ (69%), and HCl (37%) were purchased from Merck Millipore (Germany). In this study, DDW was used for both the samples preparation procedure and the experiments involving the adsorption of Ni(II).

Instruments
XRD analysis was conducted using a Philips X'pert MPD diffractometer (Eindhoven, Netherlands). The measurements were performed with Cu Ka radiation (λ = 0.1542 nm) at 45 kV and 100 mA, covering the 2θ range of 0.8° to 5.0° with a step size of 0.02° and a step time of 1 s.

FT-IR spectroscopy of the powdered samples, mixed with dried KBr, was recorded at room temperature in the spectral region of 4000 to 400 cm⁻¹ using an Avatar 370 instrument from Thermo Nicolet, USA.

Nitrogen adsorption-desorption isotherms were obtained at 77 K using a BELSORP-mini II volumetric adsorption analyzer from BEL Japan Inc., Osaka, Japan.

FESEM was performed using a MIRA3 TESCAN-XMU instrument from Kohoutovice, Czech Republic to analyze of the sample's morphology and pore structure, while TEM was conducted using a Philips CM120 microscope from Eindhoven, Netherlands. The FESEM-mapping method was employed to analyze the elemental distribution on the sample's surface.

The trace concentrations of Ni(II) in aqueous solutions were determined using an inductively coupled plasma optical emission spectrometer (ICP-OES) instrument (Optima 7300 DV) from PerkinElmer Co., USA.

Sonication was performed via SW3H ultrasonic cleaning system working at a frequency of 37 kHz. The bottles in the adsorption tests were shaken using a digital precise shaking water bath capable of adjusting time, temperature, and rotation speed.

ChemBioDraw 20.0 software was utilized for drawing chemical molecules and structures. Origin 8.6 software from Origin Lab Corporation, USA, was employed for the analysis and visualization of graphical data. Particle size distribution (PSD) calculations for N_2 adsorption were carried out using SAIEUS software (Micromeritics Instrument Corp.) with appropriate 2D-NLDFT models.

SBSG preparation from sorghum

The grass sorghum utilized in this study was obtained from a local post-harvesting mill situated in Rehann, Esfahan province, Iran. The sorghum underwent a series of preparatory steps, including rinsing with tap water to eliminate dust and sand particles, followed by drying in an electric oven at 363 K overnight. Subsequently, the dried sorghum was mechanically crushed into smaller size, subjected to multiple rinses with DDW, and then dried once more at the temperature of 363 K for 12 h.

For preparing pure silica particles, a combination of crushed sorghum (100 g) and hydrochloric acid (0.1 N, 500 mL) was introduced into a 1000-mL round-bottom flask and subjected to vigorous stirring under reflux conditions for 6 hours at a temperature of 353 K, followed by ultrasonication for 30 min at 323 K. The resulting mixture was subsequently transferred to a 1000-mL stainless steel autoclave reactor and maintained at a temperature of 393 K under a pressure of 15 lbs for 2 h [16].

At the final stage, the acid-digested sorghum underwent repeated rinsing with DDW to ensure complete removal of hydrochloric acid, followed by drying in an oven at 363 K. The sorghum was then placed in an electric muffle furnace and heated under an air atmosphere at a temperature of 873 K for 2 h. By subjecting the purified silica particles (containing 93% SiO_2) to refluxing in a 2 mol L^{-1} sodium hydroxide (NaOH) solution in water at a temperature of 343 K for a duration of 24 h, a sodium silicate (Na_2SiO_3) solution was successfully obtained.

Synthesis of BCFH-SBA-15

The synthesis procedure of SCA-bearing cyclam, 1-(3-(trimethoxysilyl)propyl)-1,4,8,11-tetraazacyclotetradecane, is according to the method reported by Guilard and co-workers[75]. The typical procedure for preparing BCFH-SBA-15 material is outlined as follows: In a Teflon-lined container with a capacity of 1000 mL, a homogeneous mixture of P123 (10.00 g) and HCl (1.6 mol L^{-1}, 380 mL) was vigorously stirred at 298 K for 20 min, while 200.0 mL of Na2SiO3 solution obtained from SHA was added dropwise. Subsequently, the mixture was supplemented with SCA-bearing cyclam, and the resulting mixture was allowed to age for one day at 233 K, followed by heating at 383 K for an additional day. Upon completion of the hydrothermal process, the mixture was gradually cooled to room temperature, filtered, and subjected to multiple washes with water and ethanol. It was then dried in an oven at 333 K, resulting in a fine white powder. The obtained powder was introduced into a round-bottom flask containing an HCl/ethanol solution, and refluxed under an air atmosphere with continuous stirring overnight. Finally, the resulting mixture was filtered using a Buchner funnel, rinsed three times with DDW and ethanol, and air-oven dried for one day at 333 K. The purified BCFH-SBA-15 material was stored in a glass bottle sealed with a screw cap.

Adsorption tests

The stock solution of Ni(II) (1000 mg L^{-1}) was prepared by dissolving a known quantity of high-purity $Ni(NO_3)_2\cdot6H_2O$ salt in DDW solvent. The solution was prepared using volumetric techniques to ensure accuracy. The concentration of the stock solution was determined based on the desired concentration range for the adsorption experiments.

To obtain the desired working concentrations for the batch adsorption experiments, appropriate dilutions were made from the stock solution. The dilutions were prepared by measuring specific volumes of the stock solution and diluting them with DDW. The dilution process was carefully executed to achieve the desired concentrations, and the final concentrations used in the experiments were documented.

The adsorption tests were carried out by adding a certain amount of the adsorbent (BCFH-SBA-15) into a 50-mL plastic bottle with a screw cap containing 20.0 mL of Ni(II) solution. The solution temperature (T), contact time (t), solution pH, and initial adsorbate concentration (C_i) were held constant at specific values based on the type of adsorption test. The plastic bottles were mechanically shaken at a fixed temperature for a given t at 180 RPM. After shaking, the solution was passed through a cellulose filter paper (Whatman 0.45 μm) to separate the adsorbent particles, and the Ni(II) concentrations in the filtrate were measured by ICP-OES instrument.

The percentage removal (Eq. 1) and adsorption capacity (Eqs. 2 and 3) as well as equations regarding different isotherm models (Eqs. 4 to 6), thermodynamics (Eqs. 7 to 9), and kinetic models (Eqs. 10 to 13) are all given in Table 1. The adsorption data underwent three repetitions, and the resulting averages were documented. Error bars were included in the adsorption graphs to represent the measurement uncertainties.

Data availability
The data that support the findings of this study are available from the corresponding author upon reasonable request.

References

1. Lee, J., Han, S. & Hyeon, T. Synthesis of new nanoporous carbon materials using nanostructured silica materials as templates. *J. Mater. Chem*. **14**, 478–486 (2004).

2. Tavasolikejani, S. & Farazin, A. The effect of increasing temperature on simulated nanocomposites reinforced with SWBNNs and its effect on characteristics related to mechanics and the physical attributes using the MDs approach. *Heliyon* **9**, e21022 (2023).

3. Serra, M., Arenal, R. & Tenne, R. An overview of the recent advances in inorganic nanotubes. *Nanoscale* **11**, 8073–8090 (2019).

4. Shi, F., Li, L., Wang, X. L., Gu, C. D. & Tu, J. P. Metal oxide/hydroxide-based materials for supercapacitors. *RSC Adv.* **4**, 41910–41921 (2014).

5. Furukawa, H., Cordova, K. E., O'Keeffe, M. & Yaghi, O. M. The chemistry and applications of metal-organic frameworks. *Science* **341**, 1230444 (2013).

6. Mohamed, M. G., El-Mahdy, A. F. M., Kotp, M. G. & Kuo, S. W. Advances in porous organic polymers: syntheses, structures, and diverse applications. *Mater. Adv.* **3**, 707–733 (2022).

7. Díez-Pascual, A. M. Nanoparticle reinforced polymers. *Polymers* **11**, 625 (2019).

8. Bayuo, J., Rwiza, M. J., Sillanpää, M. & Mtei, K. M. Removal of heavy metals from binary and multicomponent adsorption systems using various adsorbents - a systematic review. *RSC Adv.* **13**, 13052–13093 (2023).

9. Heydari, M., Jafari, M. T., Saraji, M., Soltani, R. & Dinari, M. Covalent triazine-based framework-grafted functionalized fibrous silica sphere as a solid-phase microextraction coating for simultaneous determination of fenthion and chlorpyrifos by ion mobility spectrometry. *Microchim. Acta* **188**, 4–11 (2021).

10. Tavasolikejani, S., Hosseini, S. M., Ghiaci, M., Vangijzegem, T. & Laurent, S. Copper nanoparticles embedded into nitrogen-doped carbon fiber felt as recyclable catalyst for benzene oxidation under mild conditions. *Mol. Catal.* **553**, 113736 (2024).

11. Jadhav, V., Roy, A., Kaur, K., Rai, A. K. & Rustagi, S. Recent advances in nanomaterial-based drug delivery systems. *Nano-Struct. Nano-Objects* **37**, 101103 (2024).

12. Yang, Z. et al. Chiral nanomaterials in tissue engineering. *Nanoscale* **16**, 5014–5041 (2024).

13. Tavasolikejani, S. & Farazin, A. Explore the most recent advancements in the domain of self-healing intelligent composites specifically designed for use in dentistry. *J. Mech. Behav. Biomed. Mater.* **147**, 106123 (2023).

14. Tavasolikejani, S. & Farazin, A. Fabrication and modeling of nanocomposites with bioceramic nanoparticles for rapid wound healing: an experimental and molecular dynamics investigation. *Nanomed. Res. J.* **8**, 412–429 (2023).

15. Hu, J. & Dong, M. Recent advances in two-dimensional nanomaterials for sustainable wearable electronic devices. *J. Nanobiotechnol.* **22**, 63 (2024).

16. Shirazian, S. et al. Efficient green Cr(VI) adsorbent from sorghum waste: eco-designed functionalized mesoporous silica FDU-12. *J. Colloid Interface Sci.* **664**, 667–680 (2024).

17. Bayuo, J. An extensive review on chromium (vi) removal using natural and agricultural wastes materials as alternative biosorbents. *J. Environ. Health Sci. Eng.* **19**, 1193–1207 (2021).

18. Bayuo, J., Rwiza, M. & Mtei, K. A comprehensive review on the decontamination of lead(ii) from water and wastewater by low-cost biosorbents. *RSC Adv.* **12**, 11233–11254 (2022).

19. Ciriminna, R. et al. The sol-gel route to advanced silica-based materials and recent applications. *Chem. Rev.* **113**, 6592–6620 (2013).

20. Vivero-Escoto, J. L., Huxford-Phillips, R. C. & Lin, W. Silica-based nanoprobes for biomedical imaging and theranostic applications. *Chem. Soc. Rev.* **41**, 2673–2685 (2012).

21. Hartmann, M. & Kostrov, X. Immobilization of enzymes on porous silicas – benefits and challenges. *Chem. Soc. Rev.* **42**, 6277–6289 (2013).

22. Caltagirone, C., Bettoschi, A., Garau, A. & Montis, R. Silica-based nanoparticles: a versatile tool for the development of efficient imaging agents. *Chem. Soc. Rev.* **44**, 4645–4671 (2015).

23. Gérardin, C., Reboul, J., Bonne, M. & Lebeau, B. Ecodesign of ordered mesoporous silica materials. *Chem. Soc. Rev.* **42**, 4217–4255 (2013).

24. FAOSTAT. No Title. http://faostat3.fao.org/browse/FB/*/E (2011).

25. Reynolds, M. P. et al. An integrated approach to maintaining cereal productivity under climate change. *Glob. Food Security* **8**, 9–18 (2016).

26. Mupa, M., Hungwe, C. B., Witzleben, S., Mahamadi, C. & Muchanyereyi, N. Extraction of silica gel from Sorghum bicolour (L.) moench bagasse ash. *Afr. J. Pure Appl. Chem.* **9**, 12–17 (2015).

27. Periasamy, V. S., Athinarayanan, J. & Alshatwi, A. A. Extraction and biocompatibility analysis of silica phytoliths from sorghum husk for three-dimensional cell culture. *Process. Biochem.* **70**, 153–159 (2018).

28. Sanayei, Y., Ismail, N. & Talebi, S. M. Determination of Heavy Metals in Zayandeh Rood River, Isfahan-Iran. *World Appl. Sci. J.* **6**, 1209–1214 (2009).

29. Ahangaran, F. & Navarchian, A. H. Recent advances in chemical surface modification of metal oxide nanoparticles with silane coupling agents: A review. *Adv. Colloid Interface Sci.* **286**, 102298 (2020).

30. Bae, J. A. et al. Synthesis of functionalized mesoporous material with: Various organo-silanes. *J. Nanosci. Nanotechnol.* **10**, 290–296 (2010).

31. Kango, S. et al. Surface modification of inorganic nanoparticles for development of organic-inorganic nanocomposites - A review. *Prog. Polymer Sci.* **38**, 1232–1261 (2013).

32. Zuo, B. et al. Recent Advances In The Synthesis, Surface Modifications And Applications Of Core-shell Magnetic Mesoporous Silica Nanospheres. *Chem. An Asian J.* **15**, 1248–1265 (2020).

33. Yokoi, T., Yoshitake, H. & Tatsumi, T. Synthesis of amino-functionalized MCM-41 via direct co-condensation and post-synthesis grafting methods using mono-, di- and tri-amino-organoalkoxysilanes. *J. Mater. Chem.* **14**, 951–957 (2004).

34. Cagnol, F., Grosso, D. & Sanchez, C. A general one-pot process leading to highly functionalised ordered mesoporous silica films. *Chem. Commun.* **15**, 1742–1743 (2004).

35. Soltani, R. et al. Bio-based 3D dendritic silica nanosphere: a green superior adsorbent. *J. Clean. Prod.* **335**, 130204 (2022).

36. Soltani, R., Marjani, A., Hosseini, M. & Shirazian, S. Meso-architectured siliceous hollow quasi-capsule. *J. Colloid Interface Sci.* **570**, 390–401 (2020).

37. Zhao, D. et al. Triblock copolymer syntheses of mesoporous silica with periodic 50 to 300 angstrom pores. *Science* **279**, 548–552 (1998).

38. Medeiros de Paula, G., do Nascimento Rocha de Paula, L. & Freire Rodrigues, M. G. Production of MCM-41 and SBA-15 Hybrid Silicas from Industrial Waste. *Silicon* **14**, 439–447 (2022).

39. Bhagiyalakshmi, M., Yun, L. J., Anuradha, R. & Jang, H. T. Synthesis of chloropropylamine grafted mesoporous MCM-41, MCM-48 and SBA-15 from rice husk ash: their application to CO2 chemisorption. *J. Porous Mater.* **17**, (2010).

40. Soltani, R., Marjani, A. & Shirazian, S. Facile one-pot synthesis of thiol-functionalized mesoporous silica submicrospheres for Tl(I) adsorption: Isotherm, kinetic and thermodynamic studies. *J. Hazard. Mater.* **371**, 146–155 (2019).

41. Ravikovitch, P. I., Haller, G. L. & Neimark, A. V. Density functional theory model for calculating pore size distributions: pore structure of nanoporous catalysts. *Adv. Colloid Interface Sci.* **76**, (1998).

42. Ojeda, M. L. et al. On comparing BJH and NLDFT pore-size distributions determined from N2 sorption on SBA-15 substrata. *Phys. Chem. Chem. Phys.* **5**, 1859–1866 (2003).

43. Yang, C. M., Zibrowius, B., Schmidt, W. & Schüth, F. Consecutive generation of mesopores and micropores in SBA-15. *Chem. Mater.* **15**, 3739–3741 (2003).

44. Cao, Y., Khan, A., Kurniawan, T. A., Soltani, R. & Albadarin, A. B. Synthesis of hierarchical micro-mesoporous LDH/MOF nanocomposite with in situ growth of UiO-66-(NH2)2 MOF on the functionalized NiCo-LDH ultrathin sheets and its application for thallium (I) removal. *J. Mol. Liq.* **336**, 116189 (2021).

45. Soltani, R., Marjani, A., Moguei, M. R. S., Rostami, B. & Shirazian, S. Novel diamino-functionalized fibrous silica submicro-spheres with a bimodal-micro-mesoporous network: Ultrasonic-assisted fabrication, characterization, and their application for superior uptake of Congo red. *J. Mol. Liq.* **294**, 111617 (2019).

46. Janssen, A. H., Van Der Voort, P., Koster, A. J. & De Jong, K. P. A 3D-TEM study of the shape of mesopores in SBA-15 and modified SBA-15 materials. *Chem. Commun.* **15**, 1632–1633 (2002).

47. González-López, M. E., Laureano-Anzaldo, C. M., Pérez-Fonseca, A. A., Arellano, M. & Robledo-Ortíz, J. R. A Critical overview of adsorption models linearization: methodological and statistical inconsistencies. *Separation Purification Rev.* **51**, 358–372 (2022).

48. Wang, J. & Guo, X. Adsorption kinetic models: physical meanings, applications, and solving methods. *J. Hazard. Mater.* **390**, 122156 (2020).

49. Al-Ghouti, M. A. & Da'ana, D. A. Guidelines for the use and interpretation of adsorption isotherm models: Aa review. *J. Hazard. Mater* **393**, 122383 (2020).

50. Kumar, K. V. & Sivanesan, S. Selection of optimum sorption kinetics: comparison of linear and non-linear method. *J. Hazard. Mater.* **134**, 277–279 (2006).

51. Foo, K. Y. & Hameed, B. H. Insights into the modeling of adsorption isotherm systems. *Chem. Eng. J.* **156**, 2–10 (2010).

52. Lima, E. C., Hosseini-Bandegharaei, A., Moreno-Piraján, J. C. & Anastopoulos, I. A critical review of the estimation of the thermodynamic parameters on adsorption equilibria. Wrong use of equilibrium constant in the Van't Hoof equation for calculation of thermodynamic parameters of adsorption. *J. Mol. Liq.* **273**, 425–434 (2019).

53. Lima, E. C., Adebayo, M. A. & Machado, F. M. Kinetic and equilibrium models of adsorption. *Carbon Nanomater. as Adsorbents Environ. Biol. Appl.* 33–69 (2015).

54. Langmuir, I. The adsorption of gases on plane surfaces of glass, mica and platinum. *J. Am. Chem. Soc* **40**, 1361–1403 (1918).

55. Fruendlich, H. M. F. Over the adsorption in solution. *J. Phys. Chem.* **57**, 385–471 (1906).

56. Redlich, O. & Peterson, D. L. A useful adsorption isotherm. *J. Phys. Chem.* **63**, 1024 (1959).

57. Soltani, R., Marjani, A. & Shirazian, S. A hierarchical LDH/MOF nanocomposite: Single, simultaneous and consecutive adsorption of a reactive dye and Cr(vi). *Dalt. Trans.* **49**, 5323–5335 (2020).

58. Liu, Y. & Liu, Y. J. Biosorption isotherms, kinetics and thermodynamics. *Sep. Purif. Technol.* **61**, 229–242 (2008).

59. Kundu, S. & Gupta, A. K. Arsenic adsorption onto iron oxide-coated cement (IOCC): regression analysis of equilibrium data with several isotherm models and their optimization. *Chem. Eng. J.* **122**, 93-106 (2006).

60. Chang, R. & Thoman, J. W. J. *Physical Chemistry for the Chemical Sciences* (University Science Books, 2014).

61. Atkins, P. & Paula, J. De. Physical chemistry, 9th edition (*W. H. Free. Co., New York*, 2010) https://doi.org/10.1039/C7RA01786C.

62. Bayuo, J. Decontamination of cadmium(II) from synthetic wastewater onto shea fruit shell biomass. *Appl. Water Sci.* **11**, 84 (2021).

63. Qiu, T., Zeng, Y., Ye, C. & Tian, H. Adsorption thermodynamics and kinetics of p-xylene on activated carbon. *J. Chem. Eng. Data* **57**, 1551–1556 (2012).

64. Zhou, Y. et al. Removal of crystal violet by a novel cellulose-based adsorbent: Comparison with native cellulose. *Ind. Eng. Chem. Res.* **53**, 5498–5506 (2014).

65. Gaffney, D. et al. Preparation and characterisation of a Ni2+/Co2+-cyclam modified mesoporous cellular foam for the specific immobilisation of His6-alanine racemase. *J. Mol. Catal. B Enzym.* **109**, 154–160 (2014).

66. Liang, X. & Sadler, P. J. Cyclam complexes and their applications in medicine. *Chem. Soc. Rev.* **33**, 246–266 (2004).

67. Elias, H. Kinetics and mechanism of metal complex formation with N4-donor macrocycles of the cyclam type. *Coordination Chem. Rev.* **187**, 37–73 (1999).

68. Makowska-Janusik, M., Kassiba, A., Errien, N. & Mehdi, A. Mesoporous Silica functionalized by cyclam-metal groups: spectroscopic studies and numerical modeling. *J. Inorg. Organomet. Polym. Mater.* **20**, 761–773 (2010).

69. K., L. S. About the Theory of So-called Adsorption of Soluble Substances. *Sven. Vetenskapsakad. Handingarl* **24**, 1–39 (1898).

70. Blanchard, G., Maunaye, M. & Martin, G. Removal of heavy metals from waters by means of natural zeolites. *Water Res.* **18**, 1501–1507 (1984).

71. Vaghetti, J. C. P. et al. Pecan nutshell as biosorbent to remove Cu(II), Mn(II) and Pb(II) from aqueous solutions. *J. Hazard. Mater.* **162**, 270–280 (2009).

72. Wang, L. et al. Mechanisms and reutilization of modified biochar used for removal of heavy metals from wastewater: a review. *Sci. Total Environ* **668**, 1298–1309 (2019).

73. Zare-Dorabei, R., Darbandsari, M. S., Moghimi, A., Tehrani, M. S. & Nazerdeylami, S. Synthesis, characterization and application of cyclam-modified magnetic SBA-15 as a novel sorbent and its optimization by central composite design for adsorption and

74. determination of trace amounts of lead ions. *RSC Adv*. **6**, 108477–108487 (2016).

75. Zhou, H., Luo, J. & Chen, Y. Nitrogen moieties -dominated Co–N-doped nanoparticle-modified cathodes in heterogeneous-electro-Fenton-like system for catalytic decontamination of EDTA-Ni(II). *Chemosphere* **239**, 124743 (2020).

75. Dubois, G., Tripier, R., Brandès, S., Denat, F. & Guilard, R. Cyclam complexes containing silica gels for dioxygen adsorption. *J. Mater. Chem.* **12**, 2255–2261 (2002).

76. Egbosiuba, T. C. et al. Adsorption of Cr(VI), Ni(II), Fe(II) and Cd(II) ions by KIAgNPs decorated MWCNTs in a batch and fixed bed process. *Sci. Rep.* **11**, 75 (2021).

77. Uogintė, I., Lujanienė, G. & Mažeika, K. Study of Cu (II), Co (II), Ni (II) and Pb (II) removal from aqueous solutions using magnetic Prussian blue nano-sorbent. *J. Hazard. Mater.* **369**, 226–235 (2019).

78. Pawlaczyk, M. & Schroeder, G. Efficient Removal of Ni(II) and Co(II) Ions from Aqueous Solutions Using Silica-based Hybrid Materials Functionalized with PAMAM Dendrimers. *Solvent Extr. Ion Exch.* **38**, 496–521 (2020).

79. Albayati, T. M., Sabri, A. A. & Abed, D. B. Functionalized sba-15 by amine group for removal of ni(Ii) heavy metal ion in the batch adsorption system. *Desalin. Water Treat.* **174**, 301–310 (2020).

80. Zhou, Z. et al. Preparation and adsorption characteristics of an ion-imprinted polymer for fast removal of Ni(II) ions from aqueous solution. *J. Hazard. Mater.* **341**, 355–364 (2018).

81. Kadirvelu, K., Thamaraiselvi, K. & Namasivayam, C. Adsorption of nickel(II) from aqueous solution onto activated carbon prepared from coirpith. *Sep. Purif. Technol.* **24**, 497–505 (2001).

82. Tang, B. et al. Removal of aqueous Cd(II) and Ni(II) by aminopyridine functionalized magnetic Fe3O4 nanocomposites. *J. Mol. Liq.* **331**, 115780 (2021).

83. Chatterjee, A., Basu, J. K. & Jana, A. K. Alumina-silica nano-sorbent from plant fly ash and scrap aluminium foil in removing nickel through adsorption. *Powder Technol.* **354**, 792–803 (2019).

84. Repo, E., Petrus, R., Sillanpää, M. & Warchoł, J. K. Equilibrium studies on the adsorption of Co(II) and Ni(II) by modified silica gels: One-component and binary systems. *Chem. Eng. J.* **172**, 376–385 (2011).

85. Panda, G. C., Das, S. K., Bandopadhyay, T. S. & Guha, A. K. Adsorption of nickel on husk of Lathyrus sativus: behavior and binding mechanism. *Colloids Surf. B Biointerfaces* **57**, 135–142 (2007).

86. Langmuir, I. The constitution and fundamental properties of solids and liquids. Part I. Solids. *J. Am. Chem. Soc.* **38**, 2221–2295 (1916).

87. Yuh-Shan, H. Adsorption of heavy metals erom waste streams by peat School of Chemical Engineering (The University of Birmingham, 1995).

88. Elovich, S. Y. & Zhabrova, G. M. Mechanism of the catalytic hydrogenation of ethylene on nickel. I. Kinetics of the process. *Zh. Fiz. Khimii* **13**, 1761–1775 (1939).

89. Weber, W. J. & Morris, J. C. Kinetics of Adsorption on Carbon from Solution. *J. Sanit. Eng. Div.* **89**, 31–59 (1963).

Acknowledgements

Author contributions

Wensheng Yang: Conceptualization, Writing – original draft, Validation, Methodology. Saeed Shirazian: Supervision, Formal analysis, Writing – Review & Editing, Investigation. Roozbeh Soltani: Conceptualization, Writing – original draft, Methodology, Formal analysis, Investigation. Masoud Habibi Zare: Writing – original draft, Resources, Investigation, Formal analysis.

Competing interests

The authors declare no competing interests.

Additional information

Correspondence and requests for materials should be addressed to Saeed Shirazian.

Reprints and permissions information is available at http://www.nature.com/reprints

Publisher's note Springer Nature remains neutral with regard to jurisdictional claims in published maps and institutional affiliations.